


ORIGINAL RESEARCH



Sustainable up-cycling of lead-acid battery waste for hybrid perovskite solar cells

Mariana Berruet , Institute of Materials Science and Technology Research (CONICET-UNMdP), Av. Colón 10850, 7600 Mar del Plata, Argentina

Matías A. Córdoba Dto. Electrotecnia (UNCo), Buenos Aires 1400, 8300 Neuquén, Argentina

Enzo L. Spera, Ricardo E. Marotti, and Javier C. Pereyra, Instituto de Física, Facultad de Ingeniería, UdelaR, Julio Herrera y Reissig 565, Montevideo, Uruguay

Analía V. Monti, Sol.Ar SRL, Ruta Nac. 38 Km 1304, San Fernando del Valle de Catamarca, Argentina

Kurt R. Taretto, Dto. Electrotecnia (UNCo), Buenos Aires 1400, 8300 Neuquén, Argentina; Instituto de Investigación y Desarrollo en Ingeniería de Procesos, Biotecnología y Energías Alternativas (CONICET-UNCo), Buenos Aires 1400, 8300 Neuquén, Argentina

Address all correspondence to Mariana Berruet at mberruet@fi.mdp.edu.ar
(Received: 4 March 2024; accepted: 2 August 2024)

ABSTRACT

This study explores the utilization of industry-standard methods for transforming battery-waste lead into high-purity lead iodide precursors for methylammonium lead iodide perovskite synthesis. The resulting metalorganic perovskite is suitable for optoelectronic applications, such as photovoltaic solar cells.

Despite strict regulations about the use of lead in several countries, large amounts of waste lead-acid batteries are generated worldwide every year, seriously polluting the environment, and constituting a persistent threat to human health. Here, we focus on the use of lead recycled by established industrial methods to obtain lead-halide perovskite, a highly studied material for future photovoltaic and optoelectronic technology. Recycled lead is purified to obtain a lead-iodide (PbI_2) precursor for $\text{CH}_3\text{NH}_3\text{PbI}_3$ lead-halide perovskite, where a re-crystallization route was developed to eliminate impurities and refine the PbI_2 . The refined lead-iodide enables the synthesis of high-quality $\text{CH}_3\text{NH}_3\text{PbI}_3$ perovskite thin films, which exhibit comparable photoluminescence emission and photocarrier diffusion length to those obtained from commercially available PbI_2 . This result is further corroborated by 830 mV open-circuit voltage achieved with a basic solar cell device utilizing the recycled material. Our results demonstrate that lead obtained from industrial recycling methods, together with tailored synthesis and recrystallization of lead-iodide precursor, is able to deliver optoelectronic-grade $\text{CH}_3\text{NH}_3\text{PbI}_3$ perovskite. The recycled lead thus avoids further depletion of lead from virgin natural resources, reinforcing the sustainability of this material for photovoltaic and optoelectronic technology.

Keywords waste management · recovery · purification · perovskites

Discussion

- Previous research has demonstrated the potential of utilizing battery-waste lead for the synthesis of lead-based organometallic perovskites. However, the involved methods required recycling routes that deviate from industry-standard practices. Is it possible to employ established industrial recovery techniques while maintaining the obtention of high-quality precursors?
- Adopting established industrial methods, can the resulting lead-based precursors achieve the level of purity necessary for the synthesis of optoelectronic-grade perovskites?
- Can we redirect recycled battery-waste lead towards the production of renewable energy?

Introduction

In the global pursuit of sustainable energy technology, there is a growing focus on materials innovation that offers both high efficiency and cost-effectiveness for photovoltaic¹ and light-emitting devices LED technology.² Among the leading contenders in this field, lead-based perovskite materials have demonstrated exceptional performance in solar cells as well as LED devices. So far, the perovskites delivering the best-performing devices have the chemical formula $APbX_3$, where A is a monovalent cation and X is a halide ion (either Cl-, Br- or I-). Despite the promising success of these materials, the conventional synthesis of lead-based perovskites relies on virgin, high-purity lead sources, contributing to resource depletion and environmental concerns.³ Although recycling scenarios for perovskite products based on virgin lead promise sustainability,⁴⁻⁶ the inclusion of recycled lead from other residual sources paves the way for revaluation and sustainability.

First proof-of-concept results were reported by Chen et al.,⁷ where high-purity perovskites were obtained from car battery lead, resulting in efficient $CH_3NH_3PbI_3$ (methylammonium lead iodide, MAPI) perovskite solar cells. Li et al.⁸ further demonstrated the feasibility of car battery lead by synthesizing high-purity lead acetate, leading to 17%+ efficient MAPI solar cells, while Xie et al.⁹ employed alternative purification strategies and obtained impressive solar efficiencies surpassing 20%. Inorganic perovskites are also in the scope: Hu et al. recently claimed a “self-purification” effect of $CsPbI_3$ quantum-dots based on car battery lead, demonstrating solar cells with efficiencies above 14%.¹⁰ Further efforts focused on self-sustainability possibilities for perovskite photovoltaics by recycling lead at the end of the life of perovskite solar cells, obtaining high-purity MAPI and efficient solar cells.¹¹ This idea was further pursued by Binek et al., who also recycled the fluorine-doped (FTO) tin oxide-covered glass substrate, demonstrating 13% efficient cells even after three cycles.¹² Despite these important achievements, the reported results rely on laboratory-scale recycling strategies. In our view, an important step further is to harness the potential of already existing industrial-scale lead-recovery methods proven in circular economy models that involve lead recovery, recycling, and reintroduction into the lead-acid battery value chain.

In this work, we focus on redirecting an existing industrial method for the recovery of battery-waste lead towards the preparation of lead-based precursor for the synthesis of MAPI and demonstrate that the resulting quality of MAPI films suits the quality demands for optoelectronic and photovoltaic devices. To the best of our knowledge, this is the first instance where a lead battery-based industrial method has been directly employed to produce lead as a raw material for high-quality PbI_2 synthesis. We demonstrate that by fine-tuning the PbI_2 purification process, lead recycled from batteries through existing industrial methods can deliver optoelectronic-grade MAPI perovskite.

Experimental section

Lead recovery from out-of-life batteries

The key individual process steps in the industrial recovery, melting, and refining of lead from battery recycling process are described in what follows. Figure SI1 in the Supplementary Information document depicts the flow diagram of the process. The separation of lead from plastic and the reduction of volume is achieved through a crushing process. The following step is melting in a high-temperature oven with the addition of necessary supplies such as fluxes (shell, chip, tinplate, sand, charcoal, ulexite), and lead sludge. This melting stage results in the production of metallic lead and lead sludge in the form of cones. A quantitative examination of the lead concentration in the slag is conducted. If a value greater than 4% is observed, the slag is re-processed in a subsequent melting phase. Alternatively, if the proportion is lower, it is categorized as green slag and reserved for other processes at a final disposal. The subsequent step involves purification of the contaminated metallic lead in a refining process (see Fig. SI1). Here, the refining pots are filled with lead cones. Sulfur is introduced at 320–350 °C to remove the copper that emerges to the surface, and the percentage of residual copper, tin and antimony is checked to continue the process. After the temperature rises to 640–670 °C, calcium carbonate ($CaCO_3$) is added to remove Tin. In the following step, the antimony is removed by heating the mixture to 720–750 °C and adding sodium nitrate ($NaNO_3$) and $CaCO_3$. Finally, the mixture is allowed to cool to 430 °C and a final cleaning is carried out by incorporating $NaNO_3$ and extracting the material from the surface. Samples are extracted from the lead cast for a final control (chemical analysis of lead cast is shown in Table SI1), which, once approved, proceeds to mold the ingots with a purity level of 99.9%. These refined ingots are subsequently employed in the lead iodide (PbI_2) synthesis process.

PbI_2 synthesis from battery-processed Pb

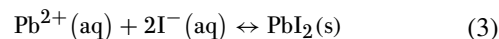
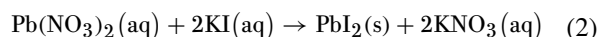
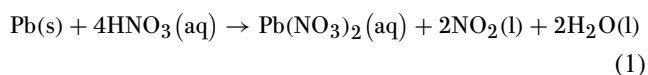
Lead nitrate ($Pb(NO_3)_2$) is synthesized by placing 100 g lead slices in a round glass matrass and slowly adding 318.2 g of concentrated nitric acid (HNO_3) over the lead. The mixture is heated gently until the lead dissolves completely, forming a transparent solution of $Pb(NO_3)_2$ (Eq. 1). In a different matrass, 165.6 g of potassium iodide (KI) is dissolved in 500 mL of distilled water to obtain a saturated solution of KI. The KI solution is slowly added to the $Pb(NO_3)_2$ solution while constantly stirring, resulting in a plum yellow color of PbI_2 (Eq. 2). The precipitate is filtered and washed with distilled water to remove any reactive in excess. PbI_2 is dried in a furnace at low temperature for several hours. The chemical analysis of impurities is showed in Table SI1.

PbI_2 purification methods

PbI_2 from the previous step is purified by recrystallization in aqueous solution to remove any impurities using two alternative methods namely at atmospheric pressure and at higher pressures

in an autoclave chamber. Henceforth, we employ the labels Atmospheric Recrystallization (AR) and Pressurized Recrystallization (PR) for the purpose of enhancing identification as shown in the rightmost labels in Fig. 1. PbI_2 is dissolved at temperature in slightly acidified water to prevent hydrolysis, and KI is added to compensate for probable iodide deficiency. The amount of additional KI is established by considering the desirable I/Pb stoichiometric ratio, the determined I/Pb ratio for PbI_2 powders (see Fig. SI2, Supplementary Information), the equilibrium displacement (Eq. 3) according to Le Chatelier principle, and the operating pressure to maximize the recrystallization performance. Consequently, the process is summarized as follows: PbI_2 at AR condition is carried out by dissolving 2 g of PbI_2 and 0.174 g of KI (Anebra ACS reagent, 99.9%) in 500 mL of deionized water (DI, 18.2 M Ω cm @ 25 °C) with 0.5 mL of acetic acid glacial (ACS reagent, \geq 99%). The solution is covered with Al foil to avoid light exposure and is heated ensuring it does not boil for at least 60 min with continuous and vigorous stirring until the PbI_2 dissolves. The supernatant is quickly transferred to a preheated conical flask and allowed to cool overnight, precipitating PbI_2 crystals. The flakes of PbI_2 are vacuum filtered, washed with DI water, and dried in a vacuum oven at 60 °C for 24 h. PbI_2 at PR condition was carried out dissolving 0.260 g of PbI_2 and 0.166 g of KI (Anebra ACS reagent, 99.9%) in 40 mL of deionized water (DI, 18.2 M Ω cm @ 25 °C) with 0.04 mL of acetic acid glacial (ACS reagent, \geq 99%) in a 50 mL Teflon-lined hydrothermal autoclave at 200 °C during 6 h. The solution is cooled slowly in the oven to reach room temperature, and the flakes of PbI_2 are filtered out in a vacuum, washed with DI water and dried in a vacuum oven at 60 °C for 24 h.

In order to compare our results with standard procedures, PbI_2 purchased from Sigma Aldrich with a purity of 99% is recrystallized and used as a reference precursor. Recrystallization at AR condition without extra KI is chosen because it is the most widely used method.^{13,14}



Preparation of methylammonium lead iodide

The precursor solution of methylammonium lead iodide (MAPI) is synthesized within a controlled environment glovebox. The solution includes a mixture of methylammonium iodide (MAI), PbI_2 from different sources (see labels in Fig. 1), and dimethyl sulfoxide (DMSO) in a molar ratio of 1:1:1 and dimethylformamide (DMF) as a solvent, 50 wt%. Briefly, MAI (Solaronix, 235 mg) and PbI_2 (B-AR, B-PR, C-AR, 681.5 mg) are mixed in DMF (1 mL) and DMSO (95 μ L). The resulting solution is then subjected to filtration using a PTFE 0.45 μ m syringe filter.

Further characterizations of MAPI films are conducted using glass and indium tin oxide (ITO) substrates. The substrates are cut into pieces of 25 \times 25 mm² and cleaned using a detergent solution, followed by rinsing with deionized water. Afterwards, the substrates are sonicated for 15 min in acetone and mixed 50:50 ethanol-isopropanol and dried using compressed air. Before the deposition step, the substrates are treated in plasma for 15 s. Immediately, the samples are transferred to a glovebox and heated at 100 °C for 5 min to evaporate residual humidity on the surface. The perovskite precursor solution is spin-coated onto the substrates at 4000 rpm for 50 s. During this step, DMF is selectively washed with chlorobenzene just before the white solid begins to crystallize in the substrate. Afterwards, the substrate is annealed at 100 °C for 10 min.

Preparation of photovoltaic devices

Photovoltaic solar cells were prepared following the layer stack Glass/FTO/c-TiO₂/mp-TiO₂/MAPI/C, where the c- and mp- prefixes indicate compact and meso-porous titanium dioxide, respectively. The FTO serves as the front contact, while

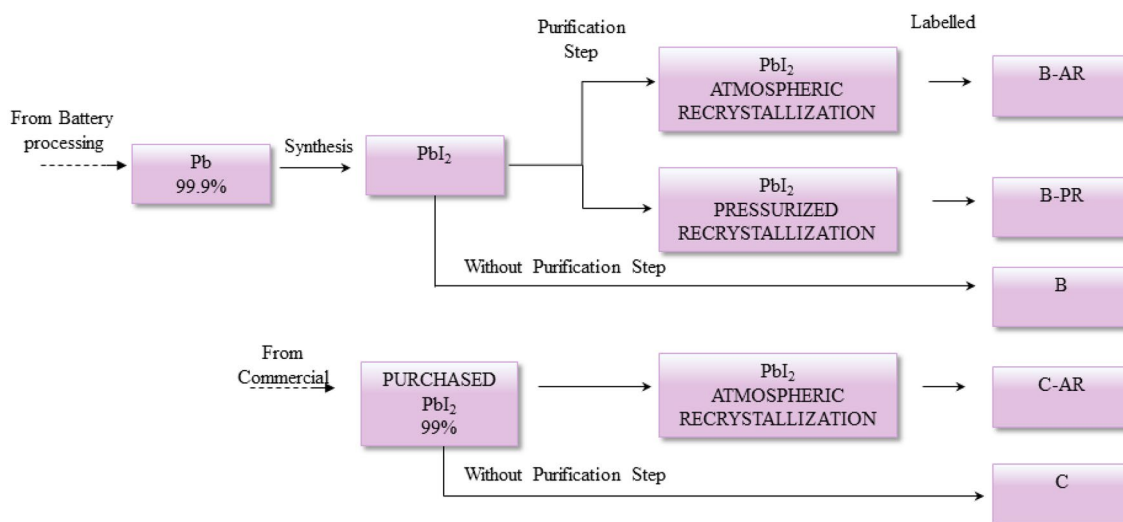


Figure 1. Further process of Lead refinement and labels in PbI_2 conditioning.

a carbon electrode was chosen for the back contact. The TiO₂ serves as an electron transport layer (ETL) for photogenerated electrons, while the corresponding photogenerated holes are transmitted directly to the carbon back contact. To isolate the effects of MAPI layers prepared with different precursors, the hole-transport layer (HTL) from the device architecture was omitted. This simplification minimizes the number of variables, facilitating a direct comparison of the MAPI layer's influence on device performance. The active area of the resulting cells is 0.1 cm². Further details about cell preparation are found in the Supplementary Information.

Characterization methods

Metal trace determination was performed by Atomic absorption spectrometry (AAS) with a Varian SpectraAA 55B instrument. X-ray diffraction (XRD) patterns were obtained with an X-ray diffractometer (Rigaku SmartLab SE), working in Bragg-Brentano geometry on a flat sample holder working at 0.0152° interval steps in the 2θ range of 10°–45° deg. Surface topography was evaluated with a Field emission scanning electron microscope (FE-SEM) (Zeiss Crossbeam 350), taking ×20,000 magnification images at 5 kV acceleration voltage.

Elemental semiquantitative analysis by X-ray fluorescence (XRF) was performed using a PW4025 Minipal2 X-ray spectrometer with a Cr anode at 20 kV and 15 μA. A complementary analysis of composition was carried out by X-ray energy dispersive spectroscopy (EDS) using an Oxford Ultimex 100 detector. X-Ray photoelectron spectroscopy (XPS) was measured with a XPS K Alpha Thermo Fisher Scientific instrument.

Thermogravimetric analysis (TGA) was performed using a Shimadzu Tga-50H instrument at a scan rate of 10 °C/min and a mixed N₂/O₂ atmosphere.

Transmittance spectra were recorded as quality assessment techniques of the samples, and different parameters such as film thickness, exciton binding energy and band gap energy were extracted by fitting (fitting model described in the Supplementary Information). The normal incidence total transmittance was measured at room temperature with S2000 OO spectrometer coupled to an integration sphere OO FOIS-1 and a HL2000 OO tungsten-halogen lamp was used as the light source.

The optoelectronic quality of the perovskite films was tested through photoluminescence (PL) measurements and the ambipolar diffusion length of photogenerated charge carriers using the steady-state photocarrier grating method (SSPG). See Supplementary Information for experimental setup details.

The SSPG technique, which has been successfully applied to different types of perovskites,^{15–17} consists of measuring the photoconductivity in a coplanar contact geometry using different non-uniform photogeneration profiles. This is accomplished by intersecting two coherent laser beams onto the film surface,¹⁸ with the intensity of one beam being much higher than the other beam (see SI in Ref. 17 for setup geometry). When biasing the sample contacts, the photoconductivity is determined in two different cases: coherent or incoherent, chosen by the polarization of one of the beams. The coherent state produces a periodic light

intensity profile on the sample and therefore a periodic photo-carrier concentration profile. Since the carriers photogenerated in the brighter semi-period smear out to the darker semi-period by diffusion, the average photoconductivity depends on the ratio between carrier diffusion length L_D to grating period Λ .¹⁹ Both polarization states yield therefore different photocurrent measurements, and the differences between currents with and without grating with respect to the current obtained with the higher intensity only, yields the ratio of current differences β , which is modeled as a function of L_D (model details given in the Supplementary Information).

Photovoltaic devices were characterized by current-voltage scans under standardized AM1.5G irradiation using an Oriel 94011A solar simulator (Xe arc lamp and AM1.5 filter) and an IVIUM CompactStat electrochemical interface. Samples were held at a forward bias voltage of 1.2 V for 10 s before sweeping the voltage down to –0.2 V, at a scan rate of 1 V/s.

Results and discussion

PbI₂ purification: Stoichiometry, thermal stability and crystal structure

The purity percentage of the raw material, Pb, and the synthesized PbI₂ (labeled as B in Fig. 1) were determined by atomic absorption spectrometry. The resultant values were 99.98% and 99.96%, respectively. In addition, chemical analysis yields the identification of metallic impurities (see chemical analysis in Table S11). The identification of traces of antimony (Sb), copper (Cu), and silver (Ag) in the lead casting acquired during battery processing, as well as copper, bismuth (Bi), and selenium (Se) in B PbI₂, requires a semi-quantitative analysis of I and Pb in the synthesized PbI₂ and subsequent purification. Table 1 presents the results of the elemental analysis of Pb and I in PbI₂ powder using EDS. Additionally, the stoichiometry can be compared with that of commercial PbI₂ as a reference (labeled as C). The PbI₂ obtained from battery processing (labeled as B, B-AR, and B-PR) exhibits a I/Pb ratio slightly higher than 2, which has been

Table 1. Energy dispersive X-ray spectroscopic analysis of PbI₂ powder.

PbI ₂	Pb (at %)	I (at %)	Another detected element (at %)	I/Pb (molar ratio)
B	32.1	65.3	2.6 (Cu)	2.037
B-AR	32.9	66.2	–	2.013
B-PR	32.6	67.4	–	2.070
C	34.3	65.7	–	1.917

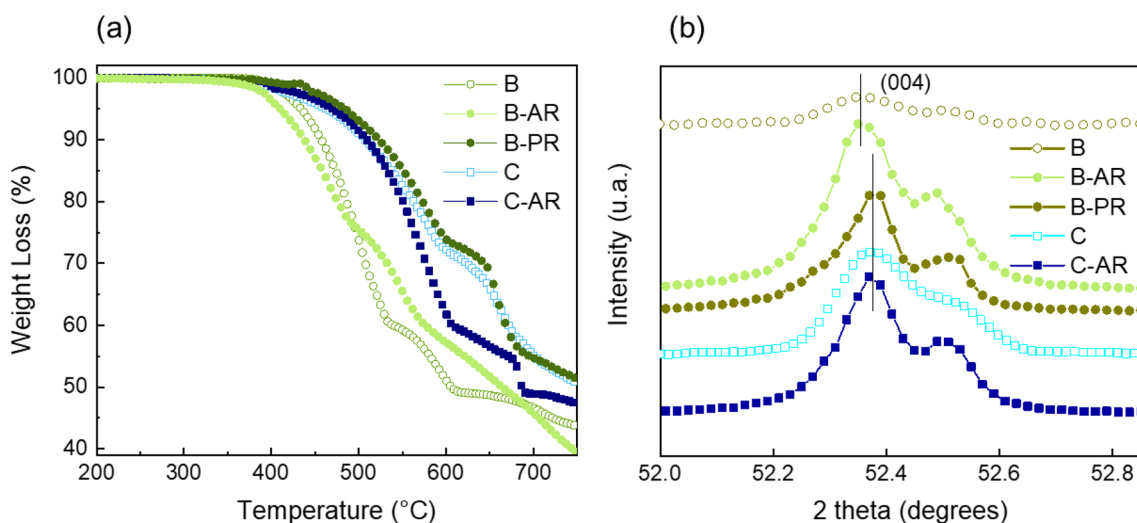


Figure 2. **a** Thermogravimetric analysis and **b** X-ray diffraction pattern of PbI_2 .

reported as suitable for PbI_2 for perovskite solar cells (PSCs).^{13,20} However, the presence of high levels of Cu in the powder without further purification (labeled as B) suggests the possibility that Cu impurities compete with Pb in the presence of KI to form CuI giving an overestimation of the iodine content associated to I-Pb binding (true I/Pb ratio). Then, the recrystallization was carried out with the addition of KI as an iodide source, considering moreover that Senevirathna et al. and Kerner et al. referred to K^+ as a beneficial additive for ionic conductivity of perovskite devices.^{14,21} With the KI addition, the recrystallization process does not only eliminate metal traces as impurities but also increases the true I/Pb ratio (see Fig. SI2).

For further details on the recrystallization processes of PbI_2 , we now analyze the results from thermogravimetric analysis (TGA). Figure 2a presents TGA curves for various PbI_2 powder samples obtained by different purification routes. Up to 400 °C, none of the PbI_2 powders exhibit a weight drop, suggesting that the crystals lack any residual H_2O or hydrated form. Subsequently, it can be observed that every sample exhibits at least two events of weight loss within the temperature range of 400–700 °C. These events align well with the decomposition of PbI_2 into metallic Pb.²² Interestingly, B-PR PbI_2 starts to lose its weight at higher temperatures than B and B-AR PbI_2 , suggesting a greater degree of thermal stability with a profile that closely resembles that of C PbI_2 . The observed improvements in thermal stability could be attributed to an enhancement in crystallinity. To verify this hypothesis, X-ray diffraction (XRD) patterns were conducted. Figure 2b shows XRD in (004) plane corresponding to the hexagonal lattice pattern (PDF 00-007-0235, ICDD 1957). Although the diffraction peaks were normalized with respect to the (001) plane due to the higher intensity if this peak (full patterns can be seen in Fig. SI3, Supplementary Information), the (004) plane was chosen for comparison between samples due to the enhanced resolution in atomic spacings at higher theta angle according to Bragg's law. As can be seen from Fig. 2b, samples B and B-AR exhibit a lower 2θ at (004) peak intensity,

indicating an increase in the interplanar distance. The observed increment in lattice constant may be responsible of the TGA profiles depicted in Fig. 2a, because as the interplanar distance is increased it requires a minor consumption of energy to break the bond between Pb–I–Pb coordination.

MAPI film characterization: Crystal structure

The XRD patterns of MAPI films deposited onto glass synthesized as described in the “Experimental section” are shown in Fig. 3. The diffractograms display clear peaks that correspond to the tetragonal symmetry of MAPI (PDF 01-084-7607, ICDD 2018). Furthermore, we identify the existence of residual PbI_2 in B-PR and B-AR samples, indicated by an asterisk in Fig. 3a. The amount of MAI and PbI_2 in each sample was the same for all methods used in this study. This suggests that the presence of PbI_2 may indicate segregation, which can be detrimental to structural as well as optoelectronic quality. Therefore, additional research will be required to clarify the impact of the relationship between MAI and battery-waste PbI_2 precursors. However, it is interesting to note that the film obtained from B-PR PbI_2 , has larger crystal domains based on the full width at half maximum (FWHM) measurement of the (110) plane of the perovskite phase (see Fig. 3b). The larger grain sizes in the B-PR sample are directly seen in top-views of SEM images (See Fig. SI4, Supplementary Information).

Figure 4 shows the results of high-resolution XPS spectra for the core levels of Pb 4f and In 3d. The photoelectron binding energy (EB) of the Pb 4f edge in Fig. 4a has a photo-peak positioned at a EB of 138.6 ± 0.1 eV and a peak splitting of 4.8 eV influenced by the halide element, agreeing with the expected signals for MAPI.²³ In the sample obtained from process B (red lines in Fig. 4), we additionally identify a signal at EB = 137 eV and a peak splitting of 4.8 eV, which corresponds to Pb^0 .²⁴

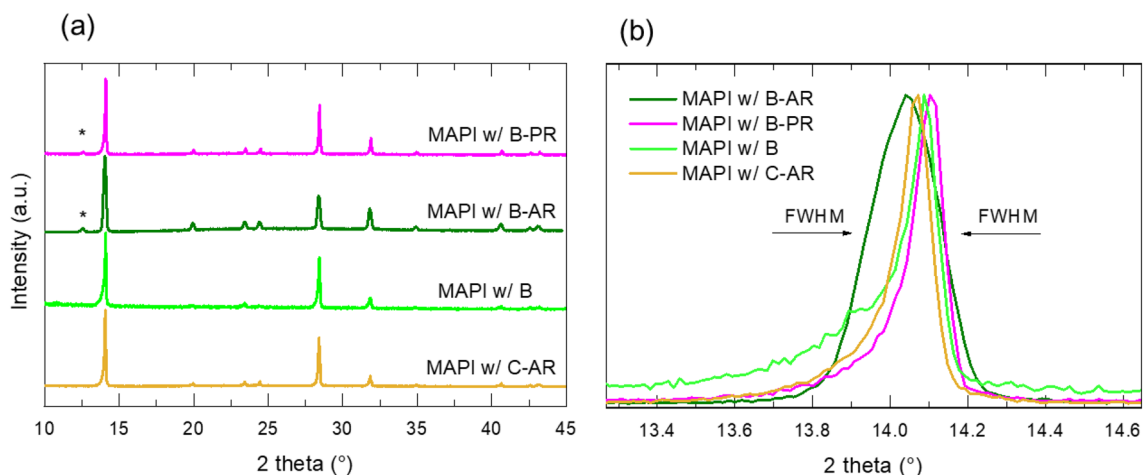


Figure 3. **a** XRD of MAPI films obtained from different sources of PbI_2 . The asterisk symbol denotes a signal attributed to PbI_2 . **b** Close-up of the peak corresponding to the (110) plane of the perovskite phase.

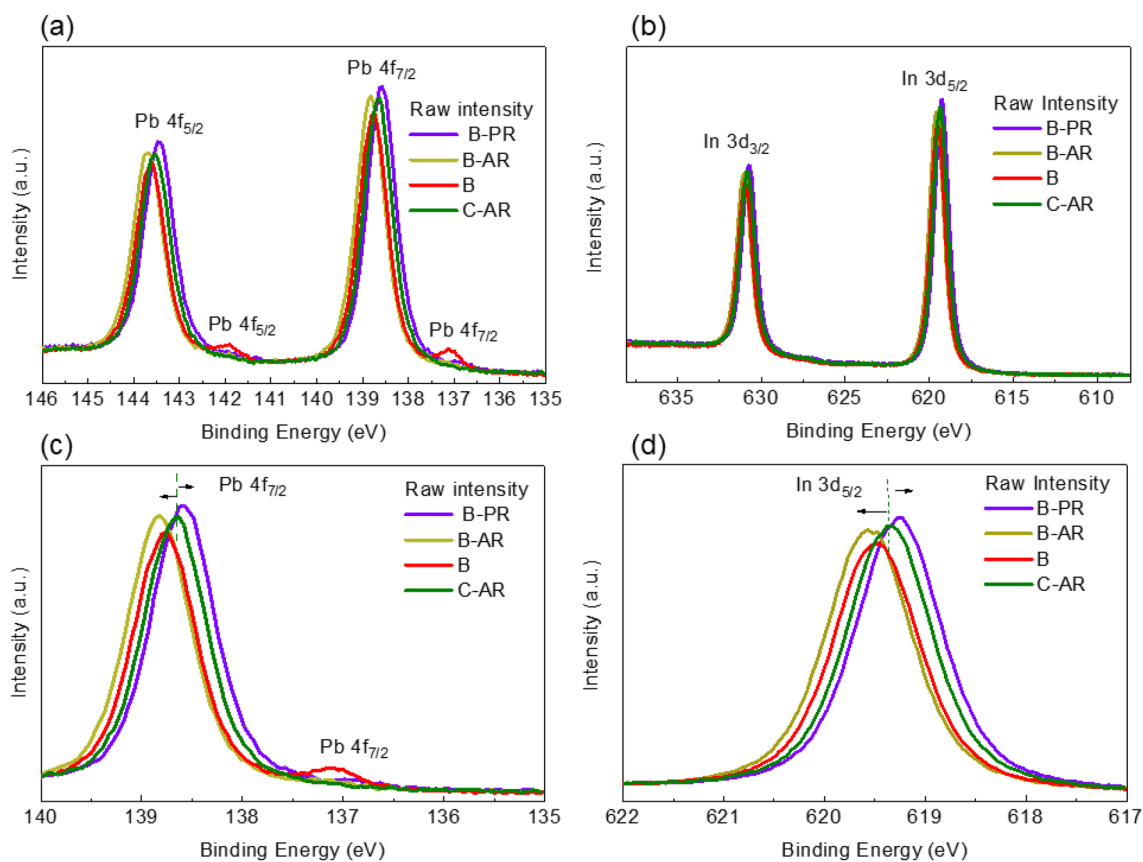


Figure 4. High-resolution XPS spectra for **a, c** Pb 4f and **b, d** In 3d core levels. C-AR MAPI was utilized as a reference to illustrate chemical shifts.

The differences in the chemical environment of the observed atomic species can be determined by tracking chemical shifts in the EB. The shifts in the Pb 4f 7/2 and In 3d 5/2 peak position, shown in higher resolution in Fig. 4c and d, reveal changes in the electron density around each atom. In the particular cases under

study, the chemical shifting could originate from the occurrence of extrinsic (or intrinsic) defects such as metallic impurities detected by AAS. The survey spectra (see Fig. SI5, Supplementary Information) did not reveal a substantial difference between films or the presence of other elements. According to the work of

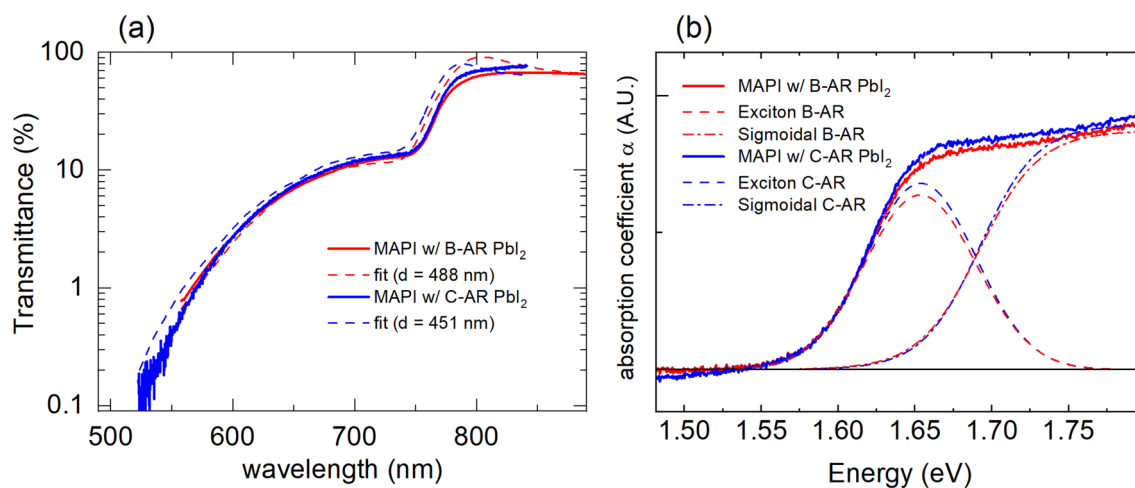


Figure 5. **a** Transmittance spectra (solid lines) of MAPI films with B-AR (red) and C-AR (blue) PbI_2 , and the corresponding fits (dashed lines) yielding the MAPI thicknesses indicated in the inset. **b** Absorbance spectra of MAPI films with B-AR (solid red) and C-AR (solid blue) PbI_2 . The dashed lines are the corresponding fitted excitonic absorption, and the dash dot lines are the corresponding fitted sigmoidal functions modeling interband absorption from Elliott's model (see Eq. S11).

Kerner et al., detrimental impurities, such as oxygen-containing anions have the potential to compete halides.¹⁴ Therefore, this will be a subject of examination in future research.

MAPI film characterization: Optical properties

Fits to the transmittance spectra yield MAPI film thicknesses in the range 450 to 490 nm (see Fig. 5a). This thickness is maintained across samples with different PbI_2 purification routes because the deposition of MAPI is carried out using the same solution and spinning parameters. The transmittance spectra are shown in logarithmic scale to appreciate the accuracy of the fits for photon energies above the band edge (wavelengths below 760 nm).

The absorption coefficient spectra of MAPI films with B-AR and C-AR PbI_2 are depicted in Fig. 5b and appears to be almost identical. The Elliott equation from Eq. S11 can be used to obtain the exciton binding energy through fitting. This energy is defined as the difference between the exciton absorption peak and the midpoint of the sigmoidal function, which represents the bandgap energy.^{25,26} Both films exhibit nearly identical exciton binding energies of 38.4 meV. Furthermore, both films have the same bandgap energy of 1.69 eV, suggesting that both exhibit identical optical absorption characteristics.

The PL spectra were divided by the integration time of the spectrometer for each measurement to make them comparable and can be seen in Fig. 6. The peak position for sample C-AR is 786 nm and for sample B-AR is 787 nm. The B-AR sample has 91% of the intensity of sample C-AR at peak position. The FWHM from the Gaussian fits is 78.6 nm for sample C-AR and 73.6 nm for sample B-AR. These findings suggest that both samples have nearly identical photoluminescence (PL) characteristics, including the same energy at which excitons recombine and the similar interaction between excitons and phonons.^{25,27} The

presence of a single clearly defined peak indicates good crystallinity in both samples. More than one peak would indicate the presence of trap states due to defects that generate exciton localized recombination along with the free exciton recombination.²⁶

MAPI film characterization: Optoelectronic quality

The optoelectronic quality of our films is deduced from measurements of the ambipolar diffusion length of photogenerated carriers by SSPG technique. Figure 7 shows the results from SSPG measurements (symbols) in terms of β vs. Λ plots, corresponding to MAPI films grown onto glass, where MAPI was obtained by the different routes adopted in this work. Figure 7a shows results for the commercial PbI_2 precursor (series C-AR), while Fig. 7b and c give the results for the atmospheric- and high-pressure crystallization routes of battery-waste PbI_2 precursors, B-AR and B-PR, respectively. The fits to the data (solid lines) yield the ambipolar diffusion length of photogenerated carriers, indicated next to each curve. Table 2 resumes the diffusion length measurements for each film type, where the displayed diffusion length corresponds to the average value from the SSPG fits from Fig. 7. The best value was obtained in the B-PR series, reaching 556 nm diffusion length. Note that since in SSPG the photogenerated carriers flow parallel to the surface, interface- as well as grain-boundary recombination affects the effective recombination lifetime. This implies that the actual intra-grain carrier diffusion length must be higher than the measured ambipolar diffusion lengths, meaning that higher diffusion lengths are to be expected in the case of carrier flow perpendicular to the surface, as in e.g., solar cells. Thus, since the diffusion length of the films from battery-waste precursor is comparable and even exceeds the film thickness 450–490 nm, we conclude that the optoelectronic quality of our films fulfills the fundamental criterion for solar cells that

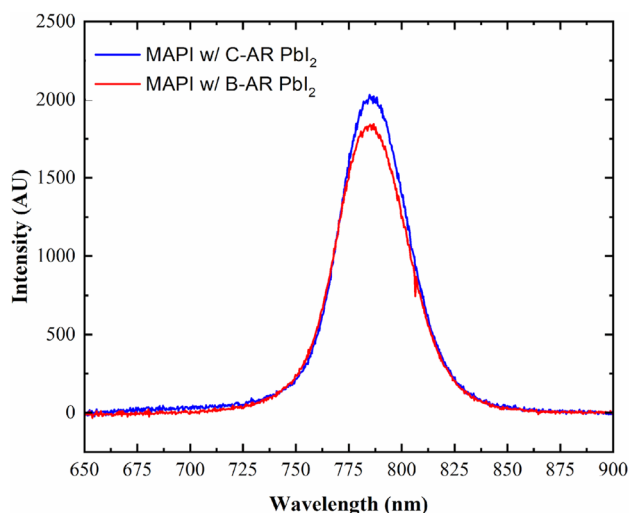


Figure 6. PL spectra for C-AR (blue) and B-AR (red) samples divided by the integration time to make them comparable.

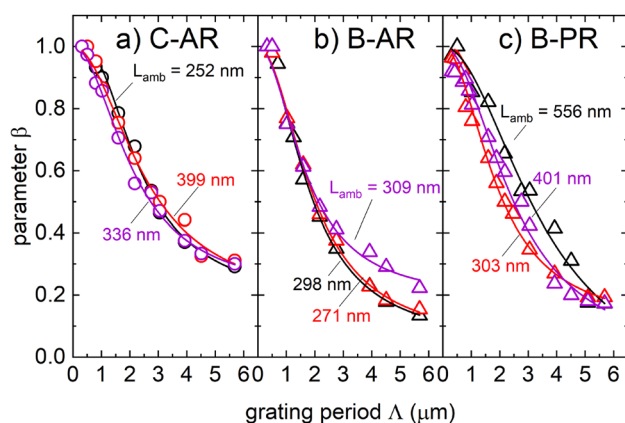


Figure 7. Experimental results (symbols) of the parameter β vs. grating period Λ obtained from SSPG measurements of three different samples in series C-AR (a), B-AR (b), and B-PR (c), and the corresponding fits (solid lines) yielding the ambipolar diffusion lengths indicated next to each curve (L_{amb}). Since the ambipolar diffusion length of series B-PR films exceeds the film thickness ($d=450$ to 490 nm), we infer that the obtained optoelectronic quality fulfills the fundamental criteria for efficient solar cells $L_{amb} > d$ (see main text for discussion).

diffusion length should exceed film thickness to attain high energy conversion efficiencies in solar cells.

MAPI film characterization: Photovoltaic devices

The characterization of solar cells prepared with commercial PbI_2 (C-AR) as well as recycled PbI_2 (B-AR) tested under standard solar illumination delivered the output parameters shown in Table 3. The corresponding current-voltage characteristics are shown in the Supplementary Information file,

Table 2. Average ambipolar diffusion length obtained from SSPG characterization of MAPI films obtained using different PbI_2 precursors or recrystallization strategies.

PbI_2	Recrystallization pressure	Designation	MAPI diffusion length L_{amb} (nm)
Commercial	Atmospheric	C-AR	329
Battery-waste	Atmospheric	B-AR	293
Battery-waste	High	B-PR	420

Table 3. Solar cell output parameters for cells prepared with commercial and refined battery-waste PbI_2 .

PbI_2	Designation	Efficiency (%)	Open-circuit voltage (mV)	Short-circuit current density (mA/cm^2)	Fill factor (%)
Commercial	C-AR	3.6	910	9.5	42
Battery-waste	B-AR	3.0	830	8.9	41

Fig. SI6 in the Supplementary Information. Despite the basic solar cell structure adopted, the achievement of 830 mV open-circuit voltages with the battery-waste precursor is indicative of a sufficiently low defect density in MAPI, in agreement with the diffusion length measurements. Such open-circuit voltages are typical for carbon-contacted MAPI solar cells without hole-transport layer.²⁸⁻³⁰ Further optimization of the device architecture, like work function tuning of the carbon electrode,³⁰ could therefore unlock higher performance devices from MAPI films prepared with battery-waste precursors.

Conclusions

We describe a feasible path from battery wastes to lead, purified lead and high purity lead iodide precursor for perovskites to lead-halide perovskite films, demonstrating that obtaining optoelectronic-grade lead-halide perovskite films is possible using battery-waste lead.

The two recrystallization processes of PbI_2 from the battery give solids without detected impurities by EDS, while the process at high pressure yields a precipitate of particles with enhanced crystallinity. The PbI_2 purification

step at atmospheric pressure leads to optoelectronic-grade $\text{CH}_3\text{NH}_3\text{PbI}_3$ perovskite films, showing nearly identical room-temperature photoluminescence than films obtained with high-purity commercial precursors. Moreover, the ambipolar diffusion length of photogenerated carriers reaches values comparable to the film thickness, implying that optoelectronic devices are possible using battery-waste precursors. Our first solar cells prepared with commercial and recycled PbI_2 showed comparable output parameters, reaching open-circuit voltages above 800 mV in a structure without hole-transport layer, which is a strong indicator for the high quality of the MAPI films obtained by the recycling process.

The obtention of optoelectronic-grade perovskite films thus shows that avoiding high-purity lead sources, contributing to alleviate resource depletion, is a viable technological path towards sustainable perovskite technology.

Acknowledgments

M. Berruet and K. Taretto acknowledge the financial support of the ANPCyT (Agencia Nacional de Promoción Científica y Tecnológica- Project PICT 4587/18) and the CIC (Comisión de Investigaciones Científicas de la Provincia de Buenos Aires - Project IP 2023). E. Spera, R. E Marotti and J. Pereyra acknowledge the partial funding provided by PEDECIBA (Programa de Desarrollo de las Ciencias Básicas) - Física, ANII (Administración Nacional de Investigación e Innovación) and the CSIC (Comisión Sectorial de Investigación Científica) and CAP (Comisión Académica de Posgrado) of the Universidad de la República, in Montevideo, Uruguay. We acknowledge Technician Martin Lere's expertise in TGA measurements, Laboratorio de Microscopía Electrónica y Análisis de Rayos X (LAMARX) and Laboratorio de Microscopía Electrónica INTEMA (LAMEI) for XPS and SEM data acquisitions, respectively. We especially thank the Argentine companies, Sol.Ar S.R.L. and Pla-Ka S.A. for data acquisition by AAS, as well as their commitment to manufacturing batteries and effectively managing the hazardous waste cycle.

Author contributions

Mariana Berruet: conceptualization, methodology, sample preparation, investigation, data curation, structural characterization, writing—original draft preparation, reviewing and editing, funding acquisition. Matías Córdoba: electronic characterization, modeling, data curation. Enzo Spera: optical characterization, modeling, data curation, writing. Ricardo Marotti: investigation, reviewing and editing, funding acquisition. Javier Pereyra: investigation, reviewing and editing. Analía Monti: methodology, sample preparation, Kurt Taretto: conceptualization, electronic characterization, modeling, writing—original draft preparation, reviewing and editing, funding acquisition, supervision.

Funding

ANPCyT (Agencia Nacional de Promoción Científica y Tecnológica- Project PICT 4587/18). CIC (Comisión de

Investigaciones Científicas de la Provincia de Buenos Aires - Project IP 2023). PEDECIBA (Programa de Desarrollo de las Ciencias Básicas) - Physics. ANII (Administración Nacional de Investigación e Innovación). CSIC (Comisión Sectorial de Investigación Científica). CAP (Comisión Académica de Posgrado).

Data availability

The authors confirm that the data supporting the findings of this study are available within the article and its supplementary materials.

Code availability

Not applicable.

Declarations

Conflict of interest

On behalf of all authors, the corresponding author states that there is no conflict of interest.

Supplementary Information

The online version contains supplementary material available at <https://doi.org/10.1557/s43581-024-00107-0>.

REFERENCES

1. J.Y. Kim, S.H. Kim, H.-H. Lee, K. Lee, W. Ma, X. Gong, A.J. Heeger, New architecture for high-efficiency polymer photovoltaic cells using solution-based titanium oxide as an optical spacer. *Adv. Mater.* **18**, 572–576 (2006). <https://doi.org/10.1002/adma.200501825>
2. G. Pacchioni, Highly efficient perovskite LEDs. *Nat. Rev. Mater.* **6**, 108–108 (2021). <https://doi.org/10.1038/s41578-021-00280-5>
3. D. O'Connor, D. Hou, Manage the environmental risks of perovskites. *One Earth* **4**, 1534–1537 (2021). <https://doi.org/10.1016/j.oneear.2021.11.002>
4. L. Serrano-Lujan, N. Espinosa, T.T. Larsen-Olsen, J. Abad, A. Urbina, F.C. Krebs, Tin- and lead-based perovskite solar cells under scrutiny: an environmental perspective. *Adv. Energy Mater.* **5**, 1501119 (2015). <https://doi.org/10.1002/aenm.201501119>
5. M. Ren, X. Qian, Y. Chen, T. Wang, Y. Zhao, Potential lead toxicity and leakage issues on lead halide perovskite photovoltaics. *J. Hazard. Mater.* **426**, 127848 (2022). <https://doi.org/10.1016/j.jhazmat.2021.127848>
6. H. Luo, P. Li, J. Ma, L. Han, Y. Zhang, Y. Song, Sustainable Pb management in perovskite solar cells toward eco-friendly development. *Adv. Energy Mater.* **12**, 2201242 (2022). <https://doi.org/10.1002/aenm.202201242>
7. P.-Y. Chen, J. Qi, M.T. Klug, X. Dang, P.T. Hammond, A.M. Belcher, Environmentally responsible fabrication of efficient perovskite solar cells from recycled car batteries. *Energy Environ. Sci.* **7**, 3659–3665 (2014). <https://doi.org/10.1039/C4EE00965G>
8. C. Li, Z. Zhu, Y. Wang, Q. Guo, C. Wang, P. Zhong, Z. Tan, R. Yang, Lead acetate produced from lead-acid battery for efficient perovskite solar cells. *Nano Energy* **69**, 104380 (2020). <https://doi.org/10.1016/j.nanoen.2019.104380>

9. L. Xie, Q. Zeng, Q. Li, S. Wang, L. Li, Z. Li, F. Liu, X. Hao, F. Hao, A green lead recycling strategy from used lead acid batteries for efficient inverted perovskite solar cells. *J. Phys. Chem. Lett.* **12**, 9595–9601 (2021). <https://doi.org/10.1021/acs.jpcclett.1c02831>
10. L. Hu, Q. Li, Y. Yao, Q. Zeng, Z. Zhou, C. Cazorla, T. Wan, X. Guan, J.-K. Huang, C.-H. Lin, M. Li, S. Cheong, R.D. Tilley, D. Chu, J. Yuan, S. Huang, T. Wu, F. Liu, Perovskite quantum dot solar cells fabricated from recycled lead-acid battery waste. *ACS Mater. Lett.* **4**, 120–127 (2022). <https://doi.org/10.1021/acsmaterialslett.1c00592>
11. S. Zhang, L. Shen, M. Huang, Y. Yu, L. Lei, J. Shao, Q. Zhao, Z. Wu, J. Wang, S. Yang, Cyclic utilization of lead in carbon-based perovskite solar cells. *ACS Sustain. Chem. Eng.* **6**, 7558–7564 (2018). <https://doi.org/10.1021/acssuschemeng.8b00314>
12. A. Binek, M.L. Petrus, N. Huber, H. Bristow, Y. Hu, T. Bein, P. Docampo, Recycling perovskite solar cells to avoid lead waste. *ACS Appl. Mater. Interfaces* **8**, 12881–12886 (2016). <https://doi.org/10.1021/acsami.6b03767>
13. C. Lee, Y. Shin, G.G. Jeon, D. Kang, J. Jung, B. Jeon, J. Park, J. Kim, S.J. Yoon, Cost-efficient, effect of low-quality PbI_2 purification to enhance performances of perovskite quantum dots and perovskite solar cells. *Energies* **14**, 201 (2021). <https://doi.org/10.3390/en14010201>
14. R.A. Kerner, E.D. Christensen, S.P. Harvey, J. Messinger, S.N. Habisreutinger, F. Zhang, G.E. Eperon, L.T. Schelhas, K. Zhu, J.J. Berry, D.T. Moore, Analytical evaluation of lead iodide precursor impurities affecting halide perovskite device performance. *ACS Appl. Energy Mater.* **6**, 295–301 (2023). <https://doi.org/10.1021/acsaem.2c02842>
15. I. Levine, S. Gupta, T.M. Brenner, D. Azulay, O. Millo, G. Hodes, D. Cahen, I. Balberg, Mobility–lifetime products in MAPbI_3 films. *J. Phys. Chem. Lett.* **7**, 5219–5226 (2016). <https://doi.org/10.1021/acs.jpcclett.6b02287>
16. C. Longeaud, F.J. Ramos, A. Rebai, J. Rousset, Impact of environmental stresses onto transport properties of hybrid perovskite investigated by steady state photocurrent grating and steady state photocurrent techniques. *Sol. RRL* **2**, 1800192 (2018). <https://doi.org/10.1002/solr.201800192>
17. M. Córdoba, M. Unmüssig, J. Herterich, U. Würfel, K. Taretto, Interpretation of slow electroluminescence and open circuit voltage transient response in Cs-based perovskite solar cells. *J. Appl. Phys.* **130**, 223101 (2021). <https://doi.org/10.1063/5.0065983>
18. J.W. Orton, P. Blood, *The Electrical Characterization of Semiconductors: Measurement of Minority Carrier Properties* (Academic Press, London, 1990)
19. I. Balberg, A.E. Delahoy, H.A. Weakliem, Self-consistency and self-sufficiency of the photocurrent grating technique. *Appl. Phys. Lett.* **53**, 992–994 (1988). <https://doi.org/10.1063/1.100051>
20. K. Tsevas, J.A. Smith, V. Kumar, C. Rodenburg, M. Fakis, A.R.B. Mohd Yusoff, M. Vasilopoulou, D.G. Lidzey, M.K. Nazeeruddin, A.D.F. Dunbar, Controlling PbI_2 stoichiometry during synthesis to improve the performance of perovskite photovoltaics. *Chem. Mater.* **33**, 554–566 (2021)
21. D.C. Senevirathna, J.C. Yu, T.A.N. Peiris, B. Li, M. Michalska, H. Li, J.J. Jasieniak, Impact of anion impurities in commercial PbI_2 on lead halide perovskite films and solar cells. *ACS Mater. Lett.* **3**, 351–355 (2021). <https://doi.org/10.1021/acsmaterialslett.1c00098>
22. T.D. Malevu, R.O. Ocaya, K.G. Tshabalala, Phase transformations of high-purity PbI_2 nanoparticles synthesized from lead-acid accumulator anodes. *Physica B* **496**, 69–73 (2016). <https://doi.org/10.1016/j.physb.2016.05.027>
23. S. Béchu, M. Ralaivisoa, A. Etcheberry, P. Schulz, Photoemission spectroscopy characterization of halide perovskites. *Adv. Energy Mater.* **10**, 1904007 (2020). <https://doi.org/10.1002/aenm.201904007>
24. J.F. Moulder, J. Chastain (eds.), *Handbook of X-Ray Photoelectron Spectroscopy: A Reference Book of Standard Spectra for Identification and Interpretation of XPS Data* (Perkin-Elmer Corporation, Eden Prairie, 1992)
25. R.J. Elliott, Intensity of optical absorption by excitons. *Phys. Rev.* **108**, 1384–1389 (1957). <https://doi.org/10.1103/PhysRev.108.1384>
26. E.L. Spera, C.J. Pereyra, D.L. Gau, M. Berruet, R.E. Marotti, Excitonic optical properties of $\text{CH}_3\text{NH}_3\text{PbI}_3$ perovskite and its dependence with temperature. *MRS Adv.* (2023). <https://doi.org/10.1557/s43580-023-00620-3>
27. S. Rudin, T.L. Reinecke, B. Segall, Temperature-dependent exciton linewidths in semiconductors. *Phys. Rev. B* **42**, 11218–11231 (1990). <https://doi.org/10.1103/PhysRevB.42.11218>
28. R. Chen, Y. Feng, C. Zhang, M. Wang, L. Jing, C. Ma, J. Bian, Y. Shi, Carbon-based HTL-free modular perovskite solar cells with improved contact at perovskite/carbon interfaces. *J. Mater. Chem. C* **8**, 9262–9270 (2020). <https://doi.org/10.1039/D0TC02226H>
29. Z. Golshani, S. Maghsoudi, S.M.A. Hosseini, Enhancement of the photovoltaic performance of HTL-free-perovskite solar cells based on carbon electrode via the modification of electron transport layer with copper oxide@polyaniline nanocomposite. *Energy Rep.* **8**, 13596–13609 (2022). <https://doi.org/10.1016/j.egy.2022.10.019>
30. Y. Gou, J. Zhang, B. Jin, W. Dai, W. Zhang, C. Chen, L. Lin, X. Wang, Q. Tai, J. Li, Work function tuning of carbon electrode to boost the charge extraction in hole transport layer-free perovskite solar cells. *Small* (2024). <https://doi.org/10.1002/sml.202403342>

Publisher's Note Springer Nature remains neutral with regard to jurisdictional claims in published maps and institutional affiliations.

Springer Nature or its licensor (e.g. a society or other partner) holds exclusive rights to this article under a publishing agreement with the author(s) or other rightsholder(s); author self-archiving of the accepted manuscript version of this article is solely governed by the terms of such publishing agreement and applicable law.